

# The effect of fluorine on reaction-rim growth dynamics in the ternary CaO-MgO-SiO<sub>2</sub> system

MEES GIJSBERT FRANKE<sup>1,\*</sup> AND BASTIAN JOACHIM-MROSKO<sup>1</sup>

<sup>1</sup>Institute of Mineralogy and Petrography, University of Innsbruck, Innrain 52f, 6020 Innsbruck, Austria

## ABSTRACT

Growth of reaction rims is mainly controlled by a change in physical parameters such as pressure and temperature, a change in the chemical composition of the system, and/or by the presence of volatiles. In particular, the effect of volatiles other than water on reaction-rim growth remains poorly understood. To accurately model metamorphic and metasomatic processes, a quantification of the effect of volatiles on reaction-rim growth dynamics is necessary but hitherto missing.

In this study, reaction rims were experimentally grown in a series of piston-cylinder experiments in the ternary CaO-MgO-SiO<sub>2</sub> system at 1000 °C and 1.5 GPa with 0–10 wt% F for 20 min. In the fluorine-free system, a rim sequence of wollastonite (Wo) | merwinite (Mer) | diopside (Di) | forsterite (Fo) | periclase (Per) formed, complying with the stable phase configuration at water-saturated conditions. As soon as 0.1 wt% F was introduced into the system, humite group minerals (HGMs) and monticellite (Mtc) appeared, resulting in the multilayer rim sequence Wo | Mer | Mtc | Fo + HGMs | Per. In experiments with fluorine concentrations  $\geq 0.5$  wt%, cuspidine (Csp) appears in the layer sequence and represents the major fluorine sink. Our data show that the addition of fluorine may stabilize the fluorine-bearing phases cuspidine and HGMs to higher temperatures, which is in agreement with previous studies (Grützner et al. 2017). However, the appearance of the nominally anhydrous minerals (NAMs) monticellite and åkermanite (Ak) at this *P-T* condition suggests that the addition of fluorine may also affect the stability of nominally fluorine-free minerals. This may be explained by the effect of fluorine on the Gibbs free energies of fluorine-bearing phases, which in turn affects the relative Gibbs free energies and thus the stabilities of all phases. An increase in absolute rim thickness from 11.8(21) to 105.6(22)  $\mu\text{m}$  (1 $\sigma$  standard deviations in parentheses) in fluorine free and 10 wt% F experiments, respectively, suggests that fluorine enhances absolute component mobilities and thus results in faster rim growth rates. Additionally, due to the presence of fluorine, a change in relative component mobilities results in microstructural changes such as a phase segregation of diopside and cuspidine at high-fluorine ( $\geq 3$  wt% F) concentrations.

These results not only imply that reaction rims may be used as a tool to infer the amount of fluorine present during metamorphic reactions but also that we need to consider the role of fluorine for a correct interpretation of the *P-T-t* history of metamorphic and metasomatic rocks.

**Keywords:** Wollastonite, cuspidine, component mobilities, palisade microstructure, metasomatic, metamorphic, volatiles, grain boundary


## INTRODUCTION

Metamorphic coronas and reaction rims are examples of a non-equilibrium net-transfer reaction, in which pre-existing mineral phases react to new phases. The growth of reaction rims is mainly controlled by a change in physical parameters such as pressure and temperature, a change in the chemical composition, and/or by the presence of volatile components, which push the system to out-of-equilibrium conditions. As the system tends to equilibrate, the interplay of reactions at the rim-reactant-interfaces and transport of chemical components across the rim control overall rim growth (Abart and Petrishcheva 2011). Reaction rims may consist of several layers, whose sequence and texture depend on the relative diffusivity of the individual chemical components in each layer (Joesten 1977). These component mobilities are, in turn, affected by parameters such as

temperature, pressure, chemical composition, and rheological properties (Milke et al. 2009; Joachim et al. 2019). This implies that an interplay of several parameters may directly influence the thickness of a reaction rim and its microstructure. Consequently, if the effect of these parameters is quantified and constrained, reaction rims have the potential to be used as a tool to gain insight into the setting and dynamics of complex geological systems.

Growth kinetics of reaction rims were repeatedly investigated in a variety of binary systems and are reasonably well understood, particularly at nominally dry conditions. Examples are the MgO-Al<sub>2</sub>O<sub>3</sub> system where spinel grows between periclase and corundum (Rossi and Fulrath 1963; Whitney and Stubican 1971; Watson and Price 2002; Götze et al. 2010; Keller et al. 2010) and the system CaCO<sub>3</sub>-SiO<sub>2</sub> where wollastonite grows between calcite and quartz (Milke and Heinrich 2002). Experimentally derived reaction rims were studied over a wide range of *P-T* conditions in the MgO-SiO<sub>2</sub> (Yund 1997; Fisler et al. 1997; Milke et al. 2001, 2007, 2009; Abart et al. 2004; Götze et al. 2010;

\* E-mail: Mees.Franke@uibk.ac.at

 Open access: Article available to all readers online. This article is CC-BY.

Gardés et al. 2011), the  $\text{Al}_2\text{O}_3$ - $\text{MgO}$  system (Götze et al. 2010), and the ternary  $\text{CaO}$ - $\text{MgO}$ - $\text{SiO}_2$  (CMS) system (Joachim et al. 2011, 2012, 2019). Recent studies even started to experimentally investigate reaction rims at high- $P$ - $T$  conditions representative for Earth's lower mantle (Nishi et al. 2013; Nagayoshi et al. 2016). However, the experimentally produced reaction rims in almost all of these studies are limited to simplified chemical systems that produce a sequence of one or a maximum of two monomineralic layers. To take the next step toward an understanding of complex natural metamorphic and metasomatic processes, we require an experimental approach that investigates the growth of multilayered rim sequences and includes volatiles.

Recent advances show that volatiles might have a major effect on the dynamics of net-transfer reactions (Yund 1997; Joachim et al. 2011, 2012, 2019; Gardés et al. 2012; Remmert et al. 2018). The presence of water, for instance, enhances the bulk diffusivity of  $\text{MgO}$  by multiple orders of magnitude in both the binary  $\text{MgO}$ - $\text{SiO}_2$  (Yund 1997; Milke et al. 2001, 2013; Gardés et al. 2012;) and the ternary CMS system (Joachim et al. 2011, 2019), thus resulting in substantially greater rim thicknesses at otherwise identical  $P$ - $T$ - $X$  conditions. The presence of small amounts of water might also affect the internal rim microstructure. For example, small amounts of surface water adsorbed on the starting materials of powdered experimental charges lead to the segregation of a biminerallite diopside + merwinite-single layered rim resulting in the formation of a merwinite–diopside–merwinite multilayered rim grown between monticellite single crystals and wollastonite matrix (Joachim et al. 2012). This reorganization of the rim microstructure can only be explained by a change in the relative cation mobilities (Abart et al. 2012). Indeed, isotopic profiles confirmed that the introduction of small amounts of water to the system increases the relative  $\text{CaO}/\text{MgO}$  mobility ratio (Joachim et al. 2019). Thus, the relation between rim microstructures and relative component mobility implies that rim microstructures may provide vital information about any physico-chemical parameters that modify the relative mobilities of chemical components.

Grain boundaries may be considered as two-dimensional defects in the crystal structure that have a high potential to host incompatible elements (Hiraga et al. 2004). It is reasonable to assume that diffusion is faster along grain boundaries than through the volume of adjacent crystals (Joesten 1991). Examples of grain boundary diffusion-controlled rim growth are the presence of wollastonite reaction rims on chert nodules (Joesten and Fisher 1988) and the growth of the double forsterite and enstatite layers grown in between periclase and quartz crystals (Gardés and Heinrich 2011). Investigation of the role of water on grain boundary characteristics may therefore provide valuable information regarding reaction-rim growth. The effect of water on intergranular diffusivity can be categorized in at least four regimes, summarized as: (1) “water-absent”: the intergranular medium is lacking any hydrous components. (2) “water-undersaturated”: a hydrous phase is incorporated in the crystal structure or adsorbed to the grain boundary. (3) “hydrous-saturated grain boundaries”: this regime is the first occurring at water-saturated conditions. (4) “interconnected fluid-filled porosity”: the grain boundaries and pores are saturated with a hydrous species, creating an interconnected network within the

granular aggregate (Farver and Yund 1995; Carlson 2010; Gardés et al. 2012). To the best of our knowledge, the classification above is solely ascribed to the  $\text{H}_2\text{O}$  content and no other volatile components were to date considered.

Although extensive research has been done to elucidate the effects of  $\text{H}_2\text{O}$  and  $\text{CO}_2$  on phase relations and component mobilities (e.g., Sterner and Pitzer 1994; Hirth and Kohlstedt 1996), much less is known about the role of other volatile compounds in the Earth's interior. In natural systems, fluids present during metamorphic and metasomatic reactions may include several other volatile components such as C, N, S, or halogens. Phase-equilibrium experiments demonstrate particularly the significance of fluorine for the stability field of fluorine-bearing minerals, where their stability is exceeded beyond the stability field of their OH-counterparts (Stalder and Ulmer. 2001; Giehl et al. 2014; Grützner et al. 2017). Additionally, experiments in the  $\text{MgO}$ - $\text{SiO}_2$ - $\text{H}_2\text{O}$ +F system showed that the fluorine salinity changes the stable humite group minerals (HGMs) assemblage (Hughes and Pawley 2019). These results demonstrate that volatiles may not only affect component mobilities but can also change phase stabilities and, therefore, the phase assemblage of metamorphic rock.

In this study, we will investigate the effect of fluorine on the growth dynamics and microstructure of a multi-layered reaction rim in the ternary CMS system and evaluate if reaction rims can be used as a tool to quantify the fluorine content of metamorphic fluids.

## METHODOLOGY

### Starting materials

Reaction rims were grown between grains and cylindrical plates of quartz and wollastonite crystals and periclase matrix with the addition of 0–10 wt% fluorine using three different setups (Fig. 1). As starting materials, we used pure synthetic  $\text{MgF}_2$  and  $\text{MgO}$  powders that were mixed thoroughly to produce a matrix with the desired fluorine fractions, natural quartz, and natural wollastonite stemming from Cziklewa near Oravitza (Banat, Romania) that was supplied by the Natural History Museum Vienna.

### Capsule assembly

For assembly “a”, clear quartz and wollastonite single crystals were crushed and individually handpicked in a grain size fraction of 500–1000  $\mu\text{m}$ , rinsed with acetone and water, and dried at 120 °C for an hour. The starting material was placed in a platinum capsule (inner diameter 2.8 mm, outer diameter 3.0 mm, length 1 cm) in alternating quartz and wollastonite layers surrounded by the powdered

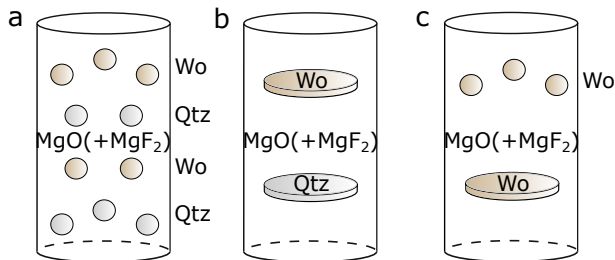


**FIGURE 1.** Schematic figure of the Pt-capsule assemblies used in this study. (a) Assembly containing four alternating layers of quartz and wollastonite grains embedded in a  $\text{MgO}+\text{MgF}_2$  powder matrix. (b) Assembly consisting of quartz and wollastonite cylinders embedded in a  $\text{MgO}+\text{MgF}_2$  powder matrix. (c) Wollastonite fragments embedded in a  $\text{MgO}+\text{MgF}_2$  powder matrix.

**TABLE 1.** Overview of the experimental conditions, assembly type, fluorine content, rim sequence, and average rim thickness

No. of experiment	Assembly type	Fluorine content (wt%)	Rim sequence	Total rim thickness $\Delta x$ ( $\mu\text{m}$ )
1.8	a	0	Wo   Mer   Di   Fo   Per	11.8(21)
1.9	a	10	Wo   Di+Csp   HGMs   Per	105.6(22)
2.1	b	1	Wo   Di+Csp+Ak   Mtc   HGMs+Fo   Per	61.6(21)
2.2	a	0.1	Wo   Mer+Di   Mtc   HGMs+Fo   Per	16.1(16)
2.3	a	5.0	Wo   Di+Csp   HGMs   Per	77.0(34)
2.6	c	0.5	Wo   Mer+Csp   Di   Mtc   Fo   Per	30.0(25)
2.9	c	0.7	Wo   Csp   Di+Mer   Mtc   HGMs+Fo   Per	35.2(20)
2.10	c	3.0	Wo   Di+Csp   HGMs   Per	59.1(13)

Notes: All experiments were performed at 1.5 GPa and 1000 °C. Uncertainties are given in terms of  $1\sigma$ .

**TABLE 2.** Composition of starting materials and phases identified in each rim sequence

Sample	CaO (wt%)	MgO (wt%)	SiO <sub>2</sub> (wt%)	F (wt%)	Total (wt%)
<b>Forsterite/HGMs</b>					
1.8	0.29(14)	58.2(14)	42.13(82)	b.d.	100.7(21)
2.2	0.79(42)	58.27(34)	38.5(10)	1.24(42)	98.77(69)
2.6	0.35(3)	58.28(28)	41.40(97)	0.13(0)	100.17(89)
2.9	0.88(15)	59.22(82)	38.9(13)	1.69(57)	100.7(12)
2.1	1.12(6)	59.8(12)	40.0(22)	1.85(54)	102.7(27)
2.10	1.2(10)	58.9(23)	29.2(30)	9.8(24)	99.19(83)
2.3	0.86(29)	58.95(31)	29.5(35)	11.0(32)	100.33(72)
1.9	1.03(15)	58.35(36)	34.22(68)	4.98(14)	98.59(93)
<b>Monticellite</b>					
2.2	35.2(11)	26.81(76)	37.73(24)	0.11(3)	99.84(74)
2.6	35.05(62)	26.28(63)	37.62(42)	0.09(5)	99.04(30)
2.9	35.21(21)	25.49(47)	37.86(57)	0.12(3)	99.68(98)
2.1	34.67(43)	26.51(58)	37.4(11)	0.16(3)	98.8(10)
<b>Diopside</b>					
1.8	26.21(13)	18.31(28)	54.62(55)	0.04(2)	99.17(67)
2.2	26.76(17)	18.38(9)	55.74(42)	0.04(4)	100.92(13)
2.6	26.50(7)	18.41(45)	54.87(40)	0.03(3)	99.82(82)
2.9	27.01(98)	18.49(46)	55.1(16)	0.06(2)	100.6(10)
2.1	26.49(26)	18.58(19)	52.96(39)	0.07(2)	98.09(30)
2.10	26.03(7)	18.63(24)	54.05(60)	0.12(2)	98.84(35)
2.3	26.17(13)	18.90(12)	55.31(43)	0.19(5)	100.57(52)
1.9	26.32(39)	18.74(34)	54.1(19)	0.17(16)	99.3(17)
<b>Akermanite</b>					
2.1	41.36(21)	14.53(14)	43.58(92)	0.07(4)	99.5(12)
<b>Merwinite</b>					
2.2	51.86(9)	12.33(9)	36.39(23)	0.11(5)	100.69(19)
2.6	49.6(22)	14.0(18)	34.75(87)	0.42(37)	98.80(96)
2.9	51.51(61)	12.60(15)	36.69(64)	0.03(2)	100.8(11)
<b>Cuspidine</b>					
2.6	58.67(68)	1.43(5)	31.34(27)	4.74(35)	96.16(65)
2.9	60.3(10)	1.4(12)	32.78(26)	7.4(11)	101.9(11)
2.1	58.0(12)	1.96(33)	31.0(16)	8.46(17)	99.42(82)
2.10	54.1(25)	4.3(13)	34.6(15)	8.46(50)	101.46(65)
2.3	50.1(42)	6.5(20)	38.3(27)	7.2(12)	102.02(78)
1.9	57.7(16)	2.30(59)	32.15(93)	9.29(57)	101.44(58)
<b>Wollastonite</b>					
	47.92(17)	0.05(1)	51.09(51)	0.01(1)	99.07(50)
<b>Quartz</b>					
	0.00(0)	0.00(0)	99.92(14)	0.00(0)	99.92(14)

Notes: Values represent averages based on at least 5 EMP point analyses. Standard deviations are given in terms of  $1\sigma$  (b.d. = below detection limit).

matrix (Fig. 1a). For assembly “b”, cylindrical plates (2 mm in diameter and 500 to 1000  $\mu\text{m}$  thick) were drilled from the quartz crystals parallel to the c-axis and polished on both sides to create flat contact surfaces with the matrix (Fig. 1b). Unoriented wollastonite cylinders were prepared in a similar way for both assembly “b” and “c”. Assembly “c” contained a combination of crushed wollastonite crystals and polished wollastonite cylinders embedded in the powdered matrix (Fig. 1c). After loading, all capsules were dried in a conventional oven at 400 °C for 30 min and welded shut subsequently with a plasma welder to minimize adsorbed surface water. A detailed overview of the experimental conditions and bulk fluorine concentrations is given in Table 1, and the composition of quartz and wollastonite starting material is shown in Table 2.

### Piston-cylinder experiments

All experiments were carried out using a conventional end-load piston-cylinder apparatus. The Pt-capsule was surrounded by MgO powder, and a talc-pyrex

assembly served as a pressure medium. Run conditions for all experiments were 1000 °C and 1.5 GPa (Fig. 2). An S-type thermo-couple was used to monitor the temperature. The target temperature was reached with a heating ramp of 30 K/min. All experiments were quenched after 20 min by cutting the power. After the run, the platinum capsule was retrieved and embedded in epoxy. Setup “a” capsules were polished until grains with a diameter between 500–1000  $\mu\text{m}$  were exposed to the surface. Setup “b” and “c” capsules were polished perpendicular to the flat surface of the cylindrical plates until the center of the respective cylinders was reached. Polished samples were cleaned with ethanol and coated with a conductive carbon film prior to SEM and microprobe analysis.

### Analytical techniques

**SEM and EMPA analyses.** BSE images were obtained with a JEOL JSM-6010LV scanning electron microscope. The rim thicknesses were determined by averaging 10 equally spaced measurements over a total distance of at least 100  $\mu\text{m}$  at places where the respective rim was thinnest (Table 1). A JEOL JXA8100 electron probe equipped with five wavelength-dispersive spectrometers was used to determine phase compositions. Mineral phases in the reaction rims were analyzed at 15 kV and 10 nA; starting materials were analyzed at 15 kV and 50 nA. Well-known standards were used for EMPA calibration. Compositions are given in Table 2 and represent the average of at least five individual analyses per phase.

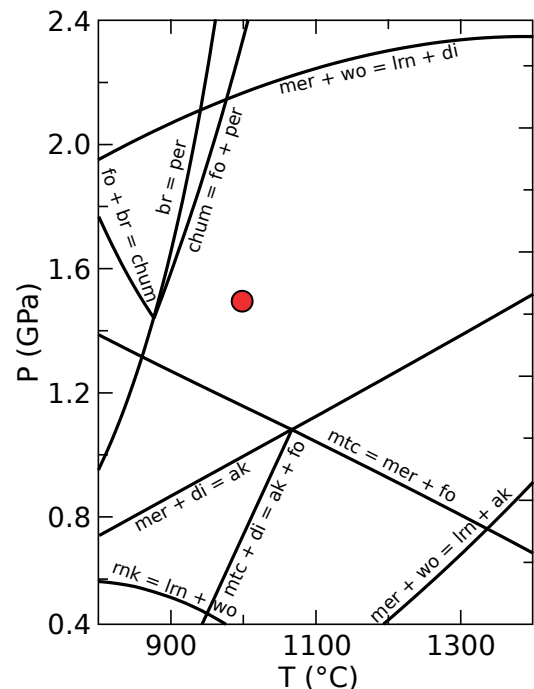


**FIGURE 2.** Pseudo-section showing the stability field of phases within the CMS ternary system at water-saturated conditions, which was created using *Perple\_X* and the *TC-DS620* version of the *Holland and Powell* database (Holland and Powell 2011). The red dot marks the experimental conditions of this study at 1000 °C and 1.5 GPa.

**Raman spectroscopy.** Raman spectroscopic analyses were performed at ambient conditions using a HORIBA JOBIN-YVON LabRam-HR800 spectrometer with a focal length of 800 mm to identify the phases in the palisade microstructure at the wollastonite interface (Figs. 3e–3h) and to distinguish HGMs in the outer layer of the reaction rim. All Raman spectra were obtained by averaging two spectra acquired for a counting time of 40 s. The analyzed areas were excited using a green Nd-YAG laser with an excitation wavelength of 532.18 nm. Scattered light was dispersed by an optical grating with 1800 grooves/mm, resulting in a spectral resolution of  $1.83\text{ cm}^{-1}$ , and collected with a cooled Andor CCD collector. An Olympus 50 $\times$  objective, a confocal pinhole of 1000  $\mu\text{m}$  and a slit of 100  $\mu\text{m}$  was used to maximize the intensity at a lateral resolution of  $\sim 5\text{ }\mu\text{m}^2$ . Before the analyses, the spectral position of the Raman mode of a Si standard wafer was measured against the position of the Rayleigh line, resulting in the expected Raman shift of  $520.7\text{ cm}^{-1}$ . Spectra were obtained in multi-window acquisition mode provided by the LABSPEC (ver. 5.93.20) software package in the frequency range of 200–1200  $\text{cm}^{-1}$ . Background subtraction and the determination of band position were performed with the same software.

## RESULTS

All experiments containing both quartz and wollastonite grains or cylinders as starting materials developed diopside layers at the original periclase-quartz interfaces. With wollastonite being the only Ca-source, this implies that the periclase-quartz interface is affected by the presence of wollastonite in the sample. Consequently, separation of quartz and wollastonite grains would be required to investigate rim growth in the binary MgO-SiO<sub>2</sub> system. Therefore, we will focus in this study on the ternary CMS system.

A series of 8 piston-cylinder experiments containing up to 10 wt% fluorine at 1000 °C and 1.5 GPa with a run duration of 20 min produced reaction rims with widths ranging between 11.8(21) and 105.6(22)  $\mu\text{m}$  (Figs. 3 and 4). Rim thicknesses were measured at localities where the total rim thickness was thinnest for geometrical reasons, and isolated rim sections with clearly visible irregularities were excluded from the data set. The occurrence of larger cracks is likely related to differential dilation during cooling and depressurization (Fig. 3) (Gardés et al. 2012). Smaller, micrometer-sized voids are often present as dark patches at the phase boundaries in the reaction rims (e.g., Figs. 3b and 3h). Phase assemblages and reaction rim widths are summarized in Table 1, and detailed analyses of phase compositions are given in Table 2. Ternary diagrams show the phase assemblage identified in rim sequences produced with 0, 0.1, 1.0, and 3.0–10 wt% F (Fig. 5).

In the fluorine-free system, a rim sequence of wollastonite (Wo) | merwinite (Mer) | diopside (Di) | forsterite (Fo) | periclase (Per) is formed at the original Wo-Per interfaces complying with phase stabilities at water-saturated conditions (Fig. 3a; see figure caption for mineral abbreviations). The reaction rim consists of two monomineralic layers of forsterite and diopside with occasional lenses of merwinite (Mer).

The addition of 0.1 wt% fluorine to the matrix produced a rim sequence of Wo | Mer | Monticellite (Mtc) | Humite Group Minerals (HGMs) + Fo | Per where diopside is sporadically present at the wollastonite interface (Fig. 3b). At 0.5 and 0.7 wt% F (Figs. 3c–3d), cuspidine (Csp) appears at the wollastonite interface in relatively small quantities, becoming more pronounced as the fluorine content increases. Raman spectroscopy analyses show the absence and reappearance of HGMs in the 0.5 and 0.7 wt% experiments, respectively (Figs. 6a and 6b). At 1 wt% F, a rim sequence of Wo | Csp + Di + Ak (åkermanite) | Mtc | HGMs + Fo | Per

is observed (Fig. 3e). The 1 wt% F experiment is the only experiment in which åkermanite is observed and also marks the disappearance of merwinite from the layer sequence. In experiments with  $\geq 1$  wt% F, palisades of diopside and cuspidine are consistently present over the entire rim (Figs. 3f–3g and 6c). In experiments with  $\geq 3$  wt% F, a layer sequence of Wo | Csp + Di | HGMs | Per is produced. Forsterite disappeared from the rim sequence where HGMs are the only phase present in the outer rim (Fig. 6d). The Di + Csp layer starts to become more irregularly oriented away from the wollastonite interface and shows a mosaic instead of palisades toward the rim-periclase interface. (Figs. 3f–3h). Furthermore, a segregation of the diopside-cuspidine palisades away from the reaction front is displayed in these reaction rims, where diopside tends to be more pronounced closer to the HGMs layer.

## DISCUSSION

### Phase configurations

In the fluorine-free system, reaction-rims between periclase and wollastonite develop the phase sequence Per | Fo | Di | Mer | Wo with merwinite being present as isolated lenses between the diopside layer and the wollastonite starting material. This phase sequence is in agreement with the stable phase configuration in the CMS system at 1000 °C, 1.5 GPa and water-saturated conditions (Holland and Powell 2011; Figs. 2, 3a, and 5a). As soon as 0.1 wt% F is introduced into the CMS system, we observe a change in the layer sequence with the appearance of monticellite and HGMs (Figs. 3b and 5b). Presence of HGMs may be explained by the fact that the stability field of F-clinohumite extends to higher temperatures compared to its OH-counterpart (Stalder and Ulmer 2001; Grützner et al. 2017; Woodland et al. 2018), which may imply that the Gibbs free energy of F-clinohumite is lower compared to OH-clinohumite at identical *P-T* conditions. However, this explanation does not hold for the presence of monticellite, which is a nominally water and fluorine-free mineral, indicating that the absolute Gibbs free energy of monticellite should remain largely unaffected by the introduction of fluorine into the system. Nevertheless, the addition of fluorine to the system may affect the Gibbs free energy difference of monticellite relative to the fluorine-bearing phases. This may result in stabilization and, consequently, the appearance of monticellite in the layer sequence.

Samples with 0.5 wt% bulk fluorine content mark the first appearance of cuspidine (Figs. 3c and 5c) while HGMs are absent (Fig. 6a). Similar to the appearance of HGMs in the experiment with 0.1 wt% F, the absolute Gibbs free energy of F-cuspidine is likely to be lowered with increasing fluorine content resulting in the appearance of this phase. Subsequently, the disappearance of HGMs between 0.1 and 0.5 wt% F may be caused by a change in relative Gibbs free energies of the potential fluorine bearing phases. Another explanation is that cuspidine as a major fluorine sink leaves insufficient fluorine for HGMs to be formed. Both explanations would be in line with the reappearance of HGMs at 0.7 wt% F (Figs. 3d, 5d, and 6b).

A further increase in the fluorine content leads to the disappearance of merwinite at 1 wt% F, followed by monticellite and åkermanite at  $\geq 3$  wt% F (Figs. 3e–3h and 5e–5f). Simultaneously, the amount of fluorine incorporated in cuspidine increases from

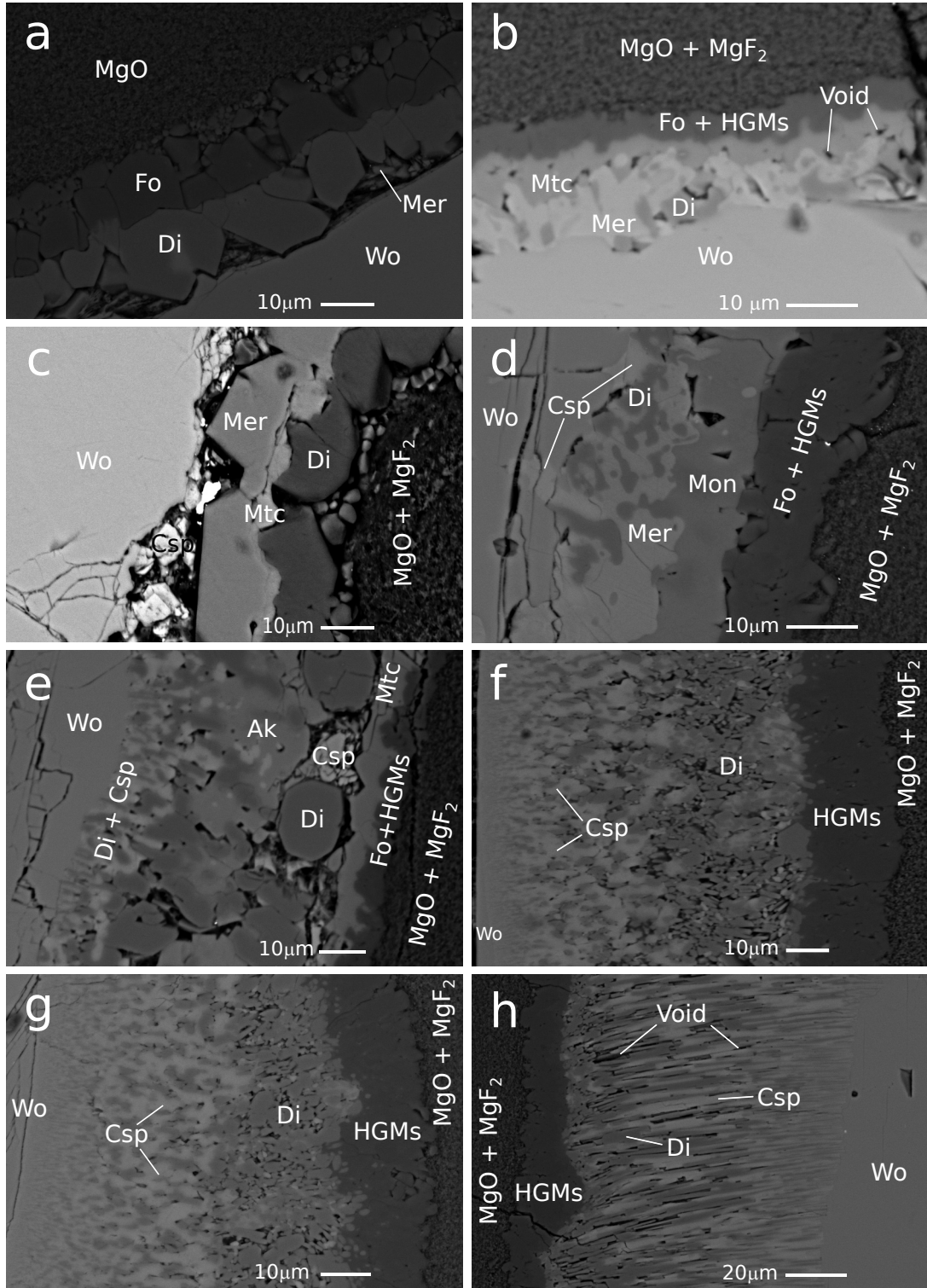


**FIGURE 3.** Scanning electron microscope (SEM) images, backscatter electron (BSE) image of reaction rims grown between wollastonite and MgO (+MgF<sub>2</sub>) matrix ordered by increasing bulk fluorine content with (a) 0, (b) 0.1, (c) 0.5, (d) 0.7, (e) 1.0, (f) 3.0, (g) 5.0, and (h) 10 wt% F. All experiments were performed at identical *P-T-t* conditions of 1000 °C and 1.5 GPa for 20 min. Rim thicknesses were always determined at the thinnest position to minimize the sectioning effect caused by a potential inclination between the grain and the matrix (Table 1). Images a and f were chosen as exemplarily visualizations of the internal rim texture and do not represent the minimum rim thickness of this specific experiment. Wo = wollastonite, Csp = cuspidine, Di = diopside, Ak = akermanite, Mer = merwinite, Mtc = monticellite, Fo = forsterite, HGMs = humite group minerals.

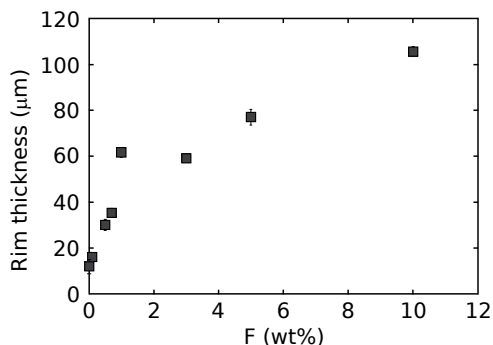


**FIGURE 4.** Plot of the overall rim thickness ( $\mu\text{m}$ ) vs. bulk fluorine content (wt%). The obtained values are an average of 10 equally spaced measurements over a region of at least  $100\ \mu\text{m}$  perpendicular to the reaction front. The grain boundaries in all experiments are most likely water saturated due to the use of a powdered matrix as starting material that introduces adsorbed surface water into the capsule (Joachim et al. 2017). Standard deviations in terms of  $1\sigma$  are denoted in the figure if they exceed the size of the symbol.

4.74(35) wt% F to 9.29(57) wt% F with increasing bulk fluorine concentration (0.5 to 10 wt% F, Table 2). Again, it seems plausible that the Gibbs free energies of the (F,OH)-bearing phases decrease with increasing fluorine content, whereas the absolute Gibbs free energies of nominally anhydrous minerals such as

merwinite, åkermanite, and monticellite, remain largely unaffected by the addition of fluorine. Consequently, the decrease in the absolute Gibbs free energy of cuspidine and HGMs can only affect the relative Gibbs Free energies of merwinite, åkermanite, and monticellite with respect to cuspidine and HGMs. This provides an explanation for the stepwise disappearance of merwinite at 1 wt% F and åkermanite and monticellite at 3 wt% F.

**Microstructural changes**

Nucleation of phases that plot on the tielines, which directly connect the starting materials wollastonite and periclase (monticellite and åkermanite; Fig. 5c), may be explained by the mobility solely of MgO or the combined mobility of CaO and SiO<sub>2</sub>. In this study, a reaction rim consisting of monomineralic layers with the sequence Wo | Mer | Di | Fo | Per develops in the fluorine-free system (Fig. 3a). Phases in this sequence deviate from the tieline that directly connects the starting materials periclase and wollastonite, which implies that additional component mobility must take place.

Several studies investigating rim growth dynamics in the binary MgO-SiO<sub>2</sub> and ternary MgO-CaO-SiO<sub>2</sub> system showed that it is the mobility of MgO that controls overall rim growth, while SiO<sub>2</sub> remains largely immobile at low-water contents (Milke et al. 2009; Gardés et al. 2012; Joachim et al. 2012, 2019). Experiments in this study were performed using dried starting materials, so that we may safely assume that at least in

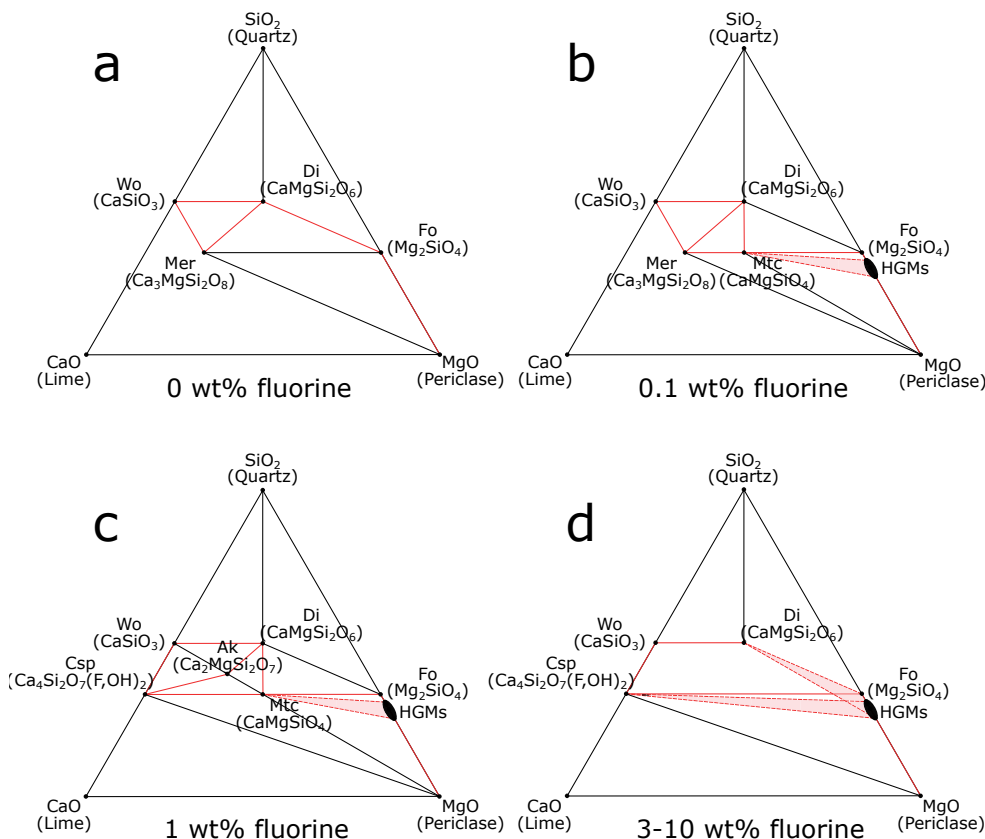


**FIGURE 5.** Ternary plots for experiments with a fluorine content of (a) 0, (b) 0.1, (c) 1, (d) 3–10 wt% F showing the phase assemblage of the rim sequences. The red lines depict phases, which are in contact with each other in the respective reaction rim.

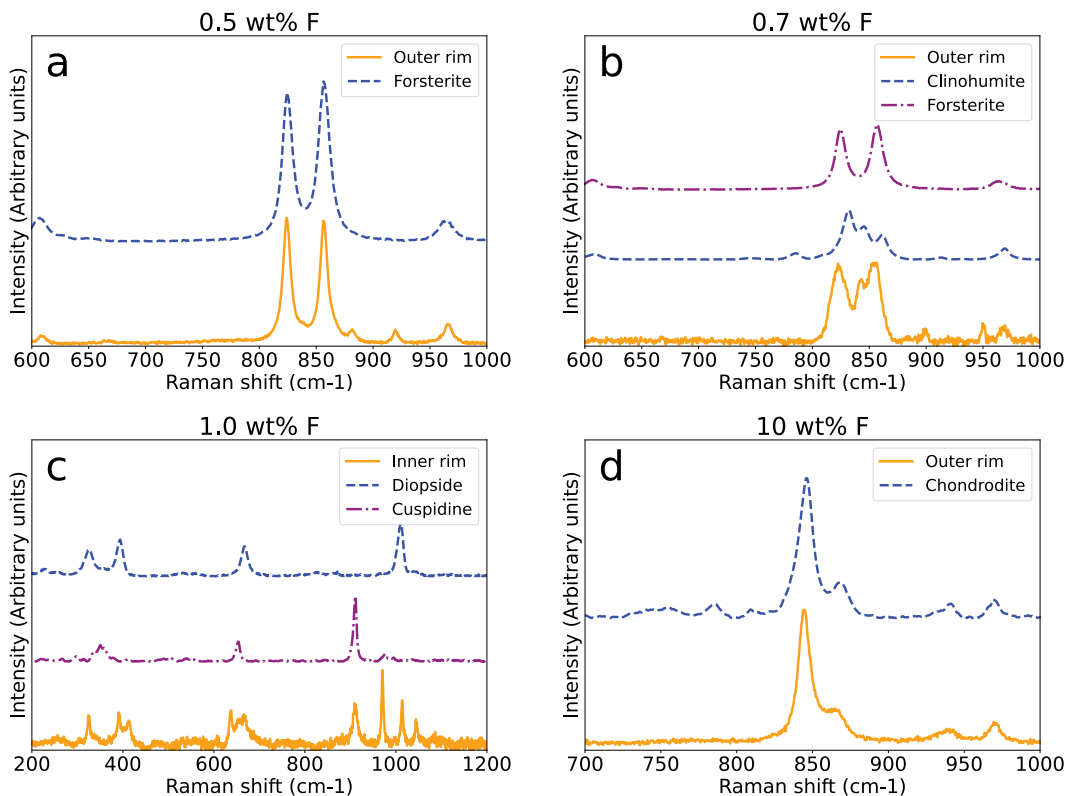
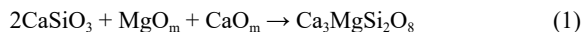
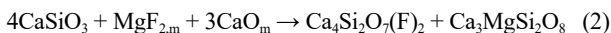


**FIGURE 6.** Representative Raman spectra of experiments with a fluorine content of 0.5 (a), 0.7 (b), 1 (c), 10 (d) wt% F. Spectra a, b, and d were taken in the outer layer of the respective rim sequence close to the rim 1 matrix interface. Spectrum c was obtained from the diopside-cuspidine palisades bordering the wollastonite interface.

the fluorine-free system the mobility of MgO controls overall rim growth. Deviation from the direct tieline connection between periclase and wollastonite requires additional mobility of at least one component. Consequently, with SiO<sub>2</sub> being most likely immobile, mobility of CaO is required to explain the phase sequence in the fluorine-free system. The mobility of CaO alone cannot contribute to overall rim growth as this would require additional mobility of SiO<sub>2</sub> (Fig. 5a) but can explain the observed phase sequence. The reaction of wollastonite to merwinite at the Wo | Mer interface in experiments with 0 and 0.1 wt% F can be written as:

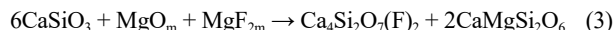


where “m” denotes a mobile component. The first appearance of cuspidine together with merwinite in the experiment with 0.5 wt% F requires additional fluorine mobility over the reaction rim, leading to the reaction:



In the sample that contains a bulk fluorine content of 0.7 wt% (Fig. 3d), a bimineralic cuspidine + diopside layer develops at the rim-wollastonite interface. At bulk fluorine concentrations of 1–3 wt%, this layer exhibits a palisade microstructure of alternating diopside and cuspidine lamellae that are oriented perpendicular to the reaction front (Figs. 3e–3h). The reaction of wollastonite to cuspidine + diopside requires the mobility of

MgO and MgF<sub>2</sub>, while the other components must remain relatively immobile. Otherwise, monomineralic layers of cuspidine and diopside would be formed instead of lamellae (Abart et al. 2012; Joachim et al. 2012). This is another argument supporting the assumption that MgO is the mobile component and thus controls overall rim growth; CaO and SiO<sub>2</sub> remain largely immobile relative to MgO because combined mobility of CaO + SiO<sub>2</sub> would result in a microstructure exhibiting monomineralic layers. The palisade growth of cuspidine and diopside at the rim-wollastonite interface can therefore be explained according to:



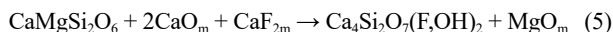
with additional CaO mobility required at the rim/reactant interface. This demonstrates that overall rim growth in the fluorine-rich systems of this study can be explained by long-range diffusion of only MgO and MgF<sub>2</sub> across the reaction rim.

In experiments with ≥3 wt% F, BSE images show a segregation of the diopside-cuspidine palisades toward the rim center, where diopside tends to be more pronounced closer to the HGMs layer and cuspidine is more pronounced at the wollastonite | rim interface (Figs. 3f–3h). Although it has been demonstrated that overall rim growth can be explained by MgO and MgF<sub>2</sub> mobility alone, segregation of diopside and cuspidine parallel to the reaction front requires additional CaO mobility. A similar observation was made by Joachim et al. (2012), who showed that the forma-

tion of a segregated multilayer type microstructure of merwinite and diopside can be explained by increasing diffusivity of either CaO or SiO<sub>2</sub>, or both, relative to MgO. We adopt this model to explain the cuspidine-diopside segregation observed in this study. Cuspidine is consumed in the outer part of the rim closer to the HGMs layer to form additional diopside according to:



The released calcium and fluorine components may migrate toward the inner part of the rim, where the complementary reaction explains the formation of cuspidine at the rim-wollastonite interface:



Note that F<sup>-</sup> may be partially substituted by OH<sup>-</sup> that was introduced into the sample as adsorbed surface water (e.g., Joachim et al. 2012).

### Growth kinetics and mass transport

Several experimental studies showed that the presence of water has a major effect on rim growth rates (Yund 1997; Milke et al. 2001, 2013; Joachim et al. 2011, 2019; Gardés et al. 2012;). This implies that a potential influence of any variations in water abundance on the results of this study must be excluded before we can discuss the effect of any other parameter on rim growth kinetics and mass transport.

A major constraint is the use of a matrix in powder form, which introduces, even if it is pre-dried, a significant amount of adsorbed water to the sample (Joachim et al. 2012). These findings are supported by Joachim et al. (2017), who demonstrate that the amount of adsorbed water introduced to a dry setup varies between 0.03 and 0.18 wt% H<sub>2</sub>O, depending on the hygroscopicity of the starting materials. The water adsorbed on the powder matrix alone is likely sufficient to reach the water-saturated grain boundary regime (Milke et al. 2013). Moreover, the growth rate of the forsterite layer in the fluorine-free system is 10<sup>-13.45(10)</sup> m<sup>2</sup>/s, which is in agreement with reported forsterite growth rates in the binary MgO-SiO<sub>2</sub> system that shows an average of 10<sup>-13.98(16)</sup> m<sup>2</sup>/s at a water content ranging from 0.11 to 0.5 wt% H<sub>2</sub>O (Gardés et al. 2012). The largest uncertainty in the determination of reaction rates is introduced through the estimation of the rim thicknesses. At very dry conditions (i.e., in regime 1), we would expect rim growth rates that are orders of magnitude slower (Gardés et al. 2012). Even when acknowledging that we compare rim growth experiments in different chemical systems here, this provides another argument that the grain boundaries of all experiments performed in this study were water saturated (regime 3, Gardés et al. 2012).

However, it seems that once grain boundaries are water saturated, significantly higher amounts of water of approximately 0.5 wt% H<sub>2</sub>O are required to further affect overall component mobilities and thereby rim growth rates (regime 4, Gardés et al. 2012). We may safely assume that the amount of adsorbed surface water introduced into the samples of this study was below this threshold, which allows us to ascribe the difference in overall rim thickness solely to the effect of fluorine. This also implies that the effect of

fluorine on component mobilities in a water-undersaturated regime cannot be evaluated in the framework of this study.

Results in this study show a positive correlation between overall rim thickness and fluorine content at otherwise identical *P-T-t-X* conditions (Fig. 4), which indicates that the bulk-rock fluorine abundance directly affects component mobilities and thus rim growth rates. This also suggests that all fluorine-bearing experiments can be assigned to transport regime 4 (Gardés et al. 2012). Additionally, the presence of micrometer-sized voids at the interfaces of adjacent phases (Figs. 3b–3h) in all fluorine-bearing experiments are potential signs of fluid transport through a network of interconnected pores, which is anticipated for regime 4 kinetics. However, the absence of 3D imaging of the pore system limits our ability to definitively prove this hypothesis.

It is important to note that even the addition of 0.1 wt% F immediately affects the overall rim growth rate. In contrast, Gardés et al. (2012), who investigated enstatite rim growth between forsterite and quartz, showed that the addition of water does not affect overall rim growth rates in regime 3, which extends to a bulk water content of 0.5 wt% H<sub>2</sub>O. One possible explanation for these contrasting observations is that the presence of fluorine already affects the grain boundary properties and thus overall component mobilities at a lower bulk fluid content compared to water. Lee et al. (1991) showed that the presence of a chlorine-bearing fluid decreases the wetting angle in low-porosity aggregates, which in turn increases the degree of fluid connectivity. If we assume that this is also valid for fluorine, this implies that the wettability of a fluorine-bearing fluid might be responsible for decreasing the wetting angle, which in turn lowers the fluid threshold necessary to create an interconnected fluid network compared to that of a pure water system. Another explanation might be that the grain and phase boundary properties of the monomineralic enstatite rims and the multilayered rim sequences observed in this study are not comparable. Both arguments illustrate that either the volatile content or the bulk chemical composition or both may affect the physicochemical characteristics of grain and phase boundaries. Therefore, it seems that the classification of intergranular mass transport in a simplified water-bearing system is not viable in a more complex fluorine-bearing system. To gain more insight into this problem, there is a need for rim-growth experiments with the addition of small, defined amounts of other volatile components.

The relative increase of the overall rim growth rate with increasing fluorine bulk concentration is strongest at low-fluorine concentrations (≤1 wt%) and decreases as the fluorine content reaches higher values (≥3 wt%, Fig. 4). Several explanations exist for this observation: (1) At high-bulk concentrations, fluorine is partially incorporated in fluorine-bearing phases such as cuspidine and HGM's, which decreases the relative fluorine availability at the grain boundaries. (2) Rims at 1 wt% bulk F show a lamellar type microstructure (Fig. 3e), while rims at 10 wt% F show a mosaic microstructure (Fig. 3h). This change in microstructure leads to a reduction in the grain boundary density normal to the reaction interface and may, as a consequence, lead to lower overall rim growth rates as suggested in previous studies (Joachim et al. 2011; Gardés et al. 2011). (3) The increase in bulk fluorine content is accompanied by a



change in the rim layer sequence (Fig. 3; see details above), which may affect grain and phase boundary properties, and subsequently, the potential effectivity of transport pathway for components through the reaction rim.

### IMPLICATIONS

Results of this study imply that fluorine may affect phase stabilities, component mobilities and the development of rim microstructures in the ternary CMS system.

The presence of fluorine significantly affects the reaction rim layer sequences and is responsible for the appearance of both fluorine-bearing minerals such as cuspidine and HGMs, and nominally fluorine-free minerals such as monticellite and åkermanite. These findings demonstrate the potential limitation of utilizing current thermodynamic data sets for phase equilibrium modeling in fluorine-bearing systems.

Absolute and relative component mobilities play a key role in net-transfer reactions because the former control the absolute rim thickness and the latter the layer sequence and microstructural features of reaction rims. This study shows that the presence of fluorine enhances the overall MgO mobility resulting in faster rim growth rates but also changes relative component mobilities in the CMS system resulting in microstructural changes such as the phase segregation of diopside and cuspidine at high-fluorine concentrations. Consequently, the results of this study emphasize the importance of taking fluorine and potentially other volatile components into consideration to accurately reconstruct the *P-T-t* history of metamorphic rocks. Further constraining and quantifying the effect of fluorine on phase stabilities and rim microstructures give natural reaction rims the potential to be used as a tool to estimate the fluorine content during their formation.

In a broader context, this implies that many features of natural reaction rims, such as the overall rim thickness, the layer sequence, the relative layer thicknesses, and the internal microstructure, contain valuable information about the respective rim forming conditions, which include not only the *P-T-t* history of a metamorphic rock but in particular the fluid-composition in fluid-mediated metasomatic reactions. Consequently, the results of this study show that natural reaction rims have the potential to serve as “geofluidometers,” which would be of great importance for samples that have lost all direct clues such as fluid inclusions that usually allow us to unravel the chemical composition of metasomatic fluids.

### ACKNOWLEDGMENTS AND FUNDING

We thank M. Tribus for her assistance with the sample preparation and microprobe analyses. We are grateful for detailed reviews by E. Gardés and an anonymous reviewer who significantly improved the quality of this paper. This research was funded by the Austrian Science Fund (FWF) project P 31787.

### REFERENCES CITED

- Abart, R., and Petrishcheva, E. (2011) Thermodynamic model for reaction-rim growth: Interface reaction and diffusion control. *American Journal of Science*, 311, 517–527.
- Abart, R., Kunze, K., Milke, R., Sperb, R., and Heinrich, W. (2004) Silicon and oxygen self-diffusion in enstatite polycrystals: The Milke et al. (2001) rim growth experiments revisited. *Contributions to Mineralogy and Petrology*, 147, 633–646.
- Abart, R., Petrishcheva, E., and Joachim, B. (2012) Thermodynamic model for growth of reaction rims with lamellar microstructure. *American Mineralogist*, 97, 231–240.
- Carlson, W.D. (2010) Dependence of reaction kinetics on H<sub>2</sub>O activity as inferred from rates of intergranular diffusion of aluminium. *Journal of Metamorphic Geology*, 28, 735–752.
- Farver, J.R., and Yund, R.A. (1995) Grain boundary diffusion of oxygen, potassium and calcium in natural and hot-pressed feldspar aggregates. *Contributions to Mineralogy and Petrology*, 118, 340–355.
- Fisler, D.K., Mackwell, S.J., and Petsch, S. (1997) Grain boundary diffusion in enstatite. *Physics and Chemistry of Minerals*, 24, 264–273.
- Gardés, E., and Heinrich, W. (2011) Growth of multilayered polycrystalline reaction rims in the MgO-SiO<sub>2</sub> system, part II: modelling. *Contributions to Mineralogy and Petrology*, 162, 37–49.
- Gardés, E., Wunder, B., Wirth, R., and Heinrich, W. (2011) Growth of multilayered polycrystalline reaction rims in the MgO-SiO<sub>2</sub> system, part I: Experiments. *Contributions to Mineralogy and Petrology*, 161, 1–12.
- Gardés, E., Wunder, B., Marquardt, K., and Heinrich, W. (2012) The effect of water on intergranular mass transport: New insights from diffusion-controlled reaction rims in the MgO-SiO<sub>2</sub> system. *Contributions to Mineralogy and Petrology*, 164, 1–16.
- Giehl, C., Marks, M.A.W., and Nowak, M. (2014) An experimental study on the influence of fluorine and chlorine on phase relations in peralkaline phonolitic melts. *Contributions to Mineralogy and Petrology*, 167, 1–21.
- Götze, L.C., Abart, R., Rybacki, E., Keller, L.M., Petrishcheva, E., and Dresen, G. (2010) Reaction rim growth in the system MgO-Al<sub>2</sub>O<sub>3</sub>-SiO<sub>2</sub> under uniaxial stress. *Mineralogy and Petrology*, 99, 263–277.
- Grützner, T., Klemme, S., Rohrbach, A., Gervasoni, F., and Berndt, J. (2017) The role of F-clinohumite in volatile recycling processes in subduction zones. *Geology*, 45, 443–446.
- Hiraga, T., Anderson, I.M., and Kohlstedt, D.L. (2004) Grain boundaries as reservoirs of incompatible elements in the Earth's mantle. *Nature*, 427, 699–703.
- Hirth, G., and Kohlstedt, D.L. (1996) Water in the oceanic upper mantle: Implications for rheology, melt extraction and the evolution of the lithosphere. *Earth and Planetary Science Letters*, 144, 93–108.
- Holland, T.J.B., and Powell, R. (2011) An improved and extended internally consistent thermodynamic dataset for phases of petrological interest, involving a new equation of state for solids. *Journal of Metamorphic Geology*, 29, 333–383.
- Hughes, L., and Pawley, A. (2019) Fluorine partitioning between humite-group minerals and aqueous fluids: implications for volatile storage in the upper mantle. *Contributions to Mineralogy and Petrology*, 174, 1–18.
- Joachim, B., Stechern, A., Ludwig, T., Konzett, J., Pawley, A., Ruziá-Hamilton, L., Clay, P.L., Burgess, R., and Ballentine, C.J. (2017) Effect of water on the fluorine and chlorine partitioning behavior between olivine and silicate melt. *Contributions to Mineralogy and Petrology. Beitrage Zur Mineralogie Und Petrologie*, 172, 15.
- Joachim, B., Gardés, E., Abart, R., and Heinrich, W. (2011) Experimental growth of åkermanite reaction rims between wollastonite and monticellite: Evidence for volume diffusion control. *Contributions to Mineralogy and Petrology*, 161, 389–399.
- Joachim, B., Gardés, E., Velickov, B., Abart, R., and Heinrich, W. (2012) Experimental growth of diopside + merwinite reaction rims: The effect of water on microstructure development. *American Mineralogist*, 97, 220–230.
- Joachim, B., Heinrich, W., Höschel, C., and Abart, R. (2019) The effect of H<sub>2</sub>O fluid on relative component mobilities in a bimineralline reaction rim in the system CaO-MgO-SiO<sub>2</sub>. *European Journal of Mineralogy*, 31, 61–72.
- Joesten, R. (1977) Evolution of mineral assemblage zoning in diffusion metasomatism. *Geochimica et Cosmochimica Acta*, 41, 649–670.
- (1991) Grain-boundary diffusion kinetics in silicate and oxide minerals. In J. Ganguly, Ed., *Diffusion, Atomic Ordering, and Mass Transport. Advances in Physical Geochemistry*, vol 8, p. 345–395. Springer.
- Joesten, R., and Fisher, G. (1988) Kinetics of diffusion-controlled mineral growth in the Christmas Mountains (Texas) contact aureole. *Geological Society of America Bulletin*, 100, 714–732.
- Keller, L.M., Götze, L.C., Rybacki, E., Dresen, G., and Abart, R. (2010) Enhancement of solid-state reaction rates by non-hydrostatic stress effects on polycrystalline diffusion kinetics. *American Mineralogist*, 95, 1399–1407.
- Lee, V.W., Mackwell, S.J., and Brantley, S.L. (1991) The effect of fluid chemistry on wetting textures in novaculite. *Journal of Geophysical Research*, 96, 10023–10037.
- Milke, R., and Heinrich, W. (2002) Diffusion-controlled growth of wollastonite rims between quartz and calcite: comparison between nature and experiment. *Journal of Metamorphic Geology*, 20, 467–480.
- Milke, R., Wiedenbeck, M., and Heinrich, W. (2001) Grain boundary diffusion of Si, Mg, and O in enstatite reaction rims: A SIMS study using isotopically doped reactants. *Contributions to Mineralogy and Petrology*, 142, 15–26.
- Milke, R., Dohmen, R., Becker, H.W., and Wirth, R. (2007) Growth kinetics of enstatite reaction rims studied on nano-scale, Part I: Methodology, microscopic observations and the role of water. *Contributions to Mineralogy and Petrology*, 154, 519–533.
- Milke, R., Abart, R., Kunze, K., Koch-Müller, M., Schmid, D., and Ulmer, P. (2009) Matrix rheology effects on reaction-rim growth I: Evidence from orthopyrox-

- ene rim growth experiments. *Journal of Metamorphic Geology*, 27, 71–82.
- Milke, R., Neusser, G., Kolzer, K., and Wunder, B. (2013) Very little water is necessary to make a dry solid silicate system wet. *Geology*, 41, 247–250.
- Nagayoshi, M., Kubo, T., and Kato, T. (2016) Experimental investigation of the kinetics of the spinel-to-garnet transformation in peridotite: A preliminary study. *American Mineralogist*, 101, 2020–2028.
- Nishi, M., Nishihara, Y., and Irifune, T. (2013) Growth kinetics of  $\text{MgSiO}_3$  perovskite reaction rim between stishovite and periclase up to 50 GPa and its implication for grain boundary diffusivity in the lower mantle. *Earth and Planetary Science Letters*, 377–378, 191–198.
- Remmert, P., Heinrich, W., Wunder, B., Morales, L., Wirth, R., Rhede, D., and Abart, R. (2018) Synthesis of monticellite–forsterite and merwinite–forsterite symplectites in the  $\text{CaO-MgO-SiO}_2$  model system: influence of temperature and water content on microstructure evolution. *Contributions to Mineralogy and Petrology*, 173, 1–17.
- Rossi, R.C., and Fulrath, R.M. (1963) Epitaxial growth of spinel by the reaction in solid state. *Journal of the American Ceramic Society*, 46, 145–149.
- Stalder, R., and Ulmer, P. (2001) Phase relations of a serpentine composition between 5 and 14 GPa: Significance of clinohumite and phase E as water carriers into the transition zone. *Contributions to Mineralogy and Petrology*, 140, 670–679.
- Sterner, S.M., and Pitzer, K.S. (1994) An equation of state for carbon dioxide valid from zero to extreme pressures. *Contributions to Mineralogy and Petrology*, 117, 362–374.
- Watson, E.B., and Price, J.D. (2002) Kinetics of the reaction  $\text{MgO-Al}_2\text{O}_3 = 3\text{MgAl}_2\text{O}_4$  and Al-Mg interdiffusion in spinel at 1200–2000 °C and 1.0 to 4.0 GPa. *Geochimica et Cosmochimica Acta*, 66, 2123–2138.
- Whitney, W.P., and Stubican, V.S. (1971) Interdiffusion studies in the system  $\text{MgOAl}_2\text{O}_3$ . *Journal of Physics and Chemistry of Solids*, 32, 305–312.
- Woodland, A.B., Bulatov, V.K., Brey, G.P., Girmis, A.V., Höfer, H.E., and Gerdes, A. (2018) Subduction factory in an ampoule: Experiments on sediment–peridotite interaction under temperature gradient conditions. *Geochimica et Cosmochimica Acta*, 223, 319–349.
- Yund, R.A. (1997) Rates of grain boundary diffusion through enstatite and forsterite reaction rims. *Contributions to Mineralogy and Petrology*, 126, 224–236.

MANUSCRIPT RECEIVED MAY 6, 2021

MANUSCRIPT ACCEPTED AUGUST 18, 2021

MANUSCRIPT HANDLED BY JUSTIN FILIBERTO